Interannual Variability of Tropospheric Moisture and Temperature and Relationships to ENSO Using COSMIC-1 GNSS-RO Retrievals

BENJAMIN R. JOHNSTON,[a] WILLIAM J. RANDEL,[a,b] AND JOHN J. BRAUN[a]

[a] *COSMIC Program Office, University Corporation for Atmospheric Research, Boulder, Colorado*
[b] *Atmospheric Chemistry Observations and Modeling Laboratory, National Center for Atmospheric Research, Boulder, Colorado*

(Manuscript received 11 November 2021, in final form 21 June 2022)

ABSTRACT: Interannual variability of tropospheric moisture and temperature are key aspects of Earth's climate. In this study, monthly mean specific humidity (q) and temperature (T) variability is analyzed using 12 years of COSMIC-1 (C1) radio occultation retrievals between 60°N and 60°S, with a focus on the tropics. C1 retrievals are relatively independent of the a priori values for q and T within the lower/middle troposphere and upper troposphere/lower stratosphere, respectively. Tropical interannual variability is dominated by El Niño–Southern Oscillation (ENSO). Systematic increases and decreases in zonal mean q and T are observed during the 2009/10 and 2015/16 El Niño events and 2007/08 and 2010/11 La Niña events, respectively. ENSO patterns in q and T are isolated using linear regression, and anomaly magnitudes increase with altitude, reaching a maximum in the upper troposphere. Upper-tropospheric q anomalies expand from the tropics into the midlatitude lower stratosphere, and the T vertical structure is consistent with a moist adiabatic response. C1 results are compared with NCAR's Whole Atmosphere Community Climate Model (WACCM), forced by observed sea surface temperatures, to evaluate model behavior in an idealized setting. WACCM ENSO variations in q and T generally show consistent behavior with C1 with somewhat smaller magnitudes. Case studies are conducted for major ENSO events during the study period. The spatial variability of q is closely aligned with outgoing longwave radiation (OLR) anomalies. For example, midtropospheric q increases over 100% and OLR decreases over 50 W m^{-2} over the central Pacific during the 2015/16 El Niño, and substantial regional q and T anomalies are observed throughout the tropics and midlatitudes for each event.

KEYWORDS: ENSO; Moisture/moisture budget; Temperature; Occultation; Climate models; Interannual variability

1. Introduction

Knowledge of tropospheric moisture and temperature variability is essential to understanding the global climate system. Tropospheric moisture is one of the key parameters driving weather and climate variability, and moisture transport plays a significant role in the global hydrological cycle (e.g., Kim et al. 2019). To accurately model current and future climate, it is crucial to understand the variability, distribution, transport, and vertical structure of tropospheric water vapor (Rieckh et al. 2018). Observations of humidity are available from various satellite observations (Chahine et al. 2006; Pougatchev et al. 2009; Tian et al. 2013; Tian and Hearty 2020) and isolated radiosonde measurements (e.g., McCarthy et al. 2009), as well as global analyses or reanalysis datasets (e.g., Hersbach et al. 2020). In this work, we study a novel set of humidity retrievals derived from Constellation Observing System for Meteorology, Ionosphere, and Climate (COSMIC) global navigation satellite system (GNSS) radio occultation (RO) measurements (Anthes et al. 2008; Ho et al. 2020). These data provide near-global coverage for monthly means spanning the period 2007–18, and this work provides an initial analysis of large-scale geophysical variability in these data.

One of the key components of tropospheric interannual variability is El Niño–Southern Oscillation (ENSO), as it is linked to variations in tropical sea surface temperatures, convection, atmospheric moisture, temperature, and circulation throughout the troposphere (e.g., Guan and Nigam 2008; Capotondi 2013). ENSO has its origins in the tropics due to coupled ocean–atmosphere dynamics and it is the dominant driver of tropical tropospheric interannual variability (e.g., Yulaeva and Wallace 1994). Strong circulation effects have also been observed in the extratropics associated with Rossby wave propagation (Trenberth et al. 2002). The warm phase of ENSO is known as El Niño while the cold phase is known as La Niña, and these two phases occur irregularly every ~2–7 years with maximum sea surface temperature (SST) anomalies typically occurring in November–December (Liou and Ravindra Babu 2020).

The impact of ENSO on temperature and precipitation has been studied extensively in past research. Positive correlations have been shown for ENSO and temperatures throughout the tropical troposphere (Yulaeva and Wallace 1994; Calvo Fernández et al. 2004). Considerable tropospheric warming occurs during El Niño, with the largest warming occurring in the eastern Pacific (Yulaeva and Wallace 1994) and the upper troposphere (Scherllin-Pirscher et al. 2012) and is attributable to anomalous heat flux from the tropical Pacific to the atmosphere (Seager et al. 2003). Interannual tropospheric temperature anomalies associated with ENSO

Supplemental information related to this paper is available at the Journals Online website: https://doi.org/10.1175/JCLI-D-21-0884.s1.

Corresponding author: Benjamin R. Johnston, bjohnston@ucar.edu

DOI: 10.1175/JCLI-D-21-0884.1

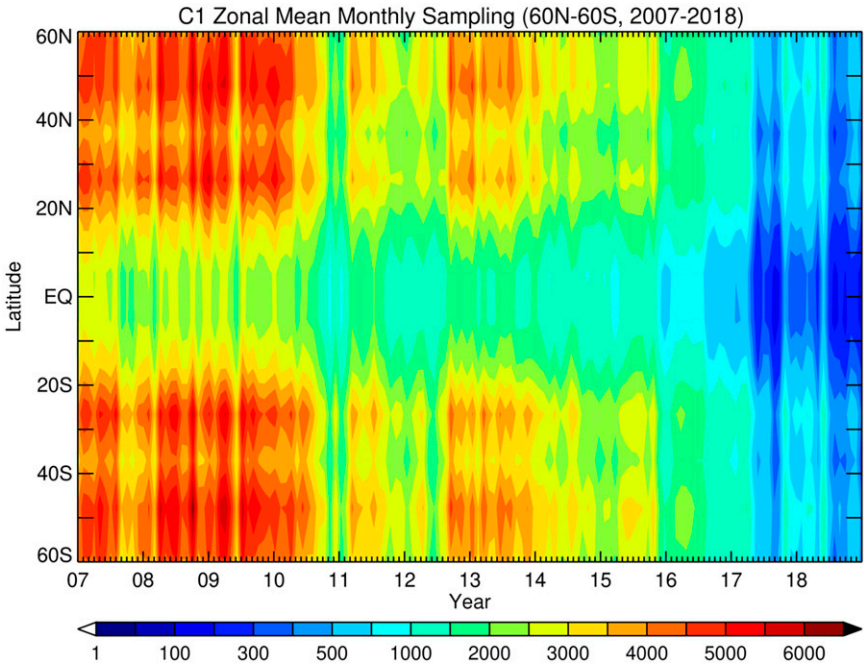

FIG. 1. C1 zonal mean monthly sampling totals within 10° latitude bands from 2007 to 2018.

also appear to be related to tropical mean SST anomalies by a simple moist adiabatic relationship (Sobel et al. 2002). While the impact of ENSO on stratospheric temperatures has not been studied as frequently, a few studies have shown that a transition from positive to negative correlations for temperature and ENSO occurs around the tropopause, with moderate cooling observed in the tropical lower stratosphere during El Niño events (Scherllin-Pirscher et al. 2012; Randel and Wu 2015). The propagation of the ENSO signal into the stratosphere has been documented into the middle and high latitudes, where ENSO is able to modify the stratospheric mean meridional circulation, also known as the Brewer–Dobson circulation (Calvo et al. 2010).

ENSO also produces significant changes in precipitation patterns around the globe. For example, warm SST anomalies produce increases in precipitation over the equatorial central and eastern Pacific and western Indian Ocean, while precipitation decreases are found to the north and south of the enhanced precipitation region as well as near the Maritime Continent (Ropelewski and Halpert 1987; Chou and Lo 2007; Yun et al. 2021). These precipitation anomalies are associated with a strengthening of the Hadley circulation and anomalous diabatic forcing of the global atmosphere circulation (Seager et al. 2003). In the midlatitudes, a prominent zonally symmetric component in precipitation patterns has been shown to occur due to tropically forced changes in the subtropical jets (Seager et al. 2005). Many of these studies have focused on the lag between the response of the tropical atmosphere and ENSO as well, with maximum correlations between ENSO indices and temperature/precipitation occurring at a lag of 2–6 months, depending on the datasets used (Trenberth et al. 2002; Calvo Fernández et al. 2004; Compo and Sardeshmukh 2010; Zheng et al. 2015; Randel and Wu 2015). This lagged atmospheric response to SST forcing has been shown to depend on the oceanic mixed layer depth, the ENSO SST forcing period, the areal fraction of the mixed layer ocean, and the strength of tropics-to-midlatitude transport (Su et al. 2005). In contrast, fewer studies have been conducted on changes in tropospheric moisture due to ENSO. Liang et al. (2011) identified the interannual signal of ENSO and described the connection between tropospheric and stratospheric water vapor, Teng et al. (2013) documented links of ENSO to variations in precipitable water and precipitation rates over the ocean, Llamedo et al. (2017) identified ENSO-related moisture anomalies near South America, and Tian et al. (2019) quantified the impact that ENSO has on tropical upper-tropospheric water vapor variance. However, it is still necessary to better characterize interannual moisture variability on a more global scale and to quantify variability throughout the entire troposphere.

Global Navigation Satellite System Radio Occultation (GNSS-RO) observations from various missions have been used in many aspects of climate research over the past two decades (Ho et al. 2020). Specifically, the joint U.S.–Taiwan six-satellite FORMOSAT-3/COSMIC (FORMOSA Satellite Series No. 3/Constellation Observing System for Meteorology, Ionosphere, and Climate, henceforth abbreviated C1) mission, launched in 2006, provides a long data record of temperature and moisture profiles. These data are characterized by high accuracy and precision, high vertical resolution, insensitivity to clouds and precipitation, and global coverage distributed relatively evenly in time and space (Anthes et al. 2008), making C1 an ideal choice for climate variability studies. Previous studies have demonstrated the value of C1 data for understanding the climate system, such as from analyzing the vertical and spatial

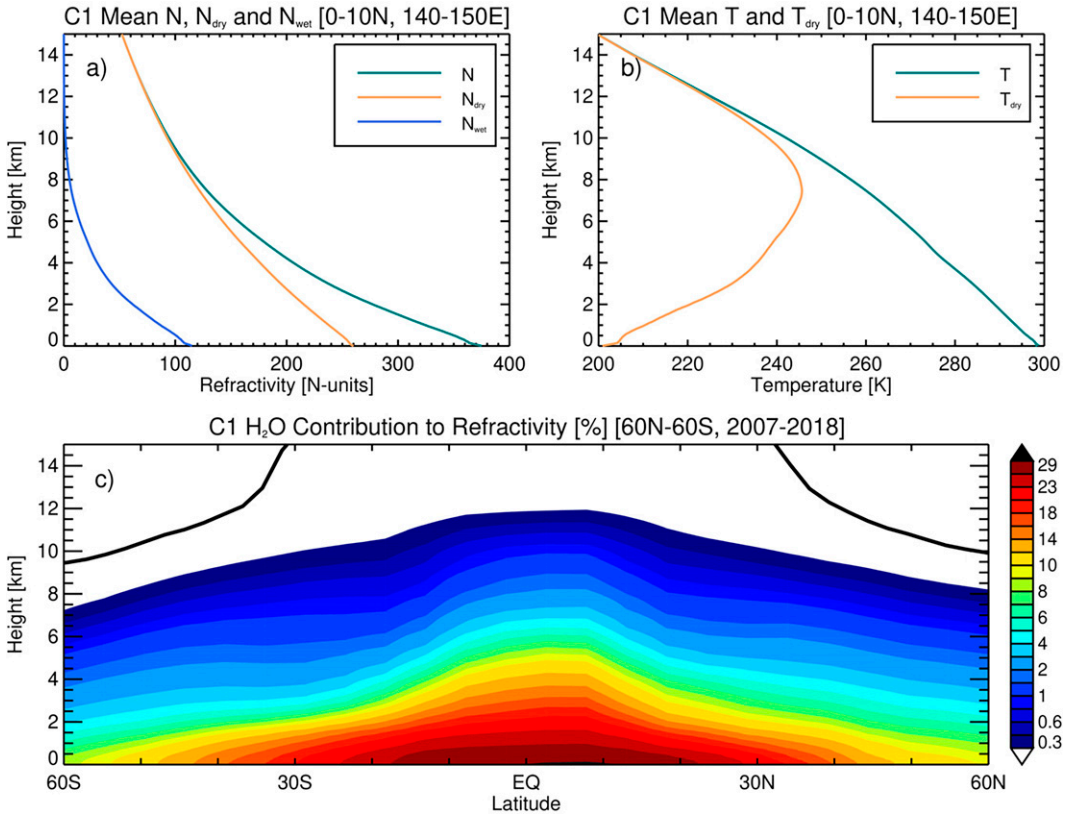

FIG. 2. (a) Contribution of the dry neutral atmosphere N_{dry} and water vapor N_{wet} to the C1 mean refractivity profile within 0°–10°N, 140°–150°E. (b) Mean temperature and dry temperature (K) within the same region. (c) Zonal mean contribution of water vapor to the C1 mean refractivity profile (%) within 60°N–60°S from 2007 to 2018. Tropopause heights are denoted by the solid black line.

structure of temperatures during ENSO (Scherllin-Pirscher et al. 2012), examining atmospheric diurnal variability (Xie et al. 2010), describing upper-troposphere and lower-stratosphere (UTLS) temperature anomalies due to the Madden–Julian oscillation (MJO) (Tian et al. 2012), estimating tropopause height variability and trends in relation to ENSO (Gao et al. 2015), and quantifying the effects of deep convection on the surrounding temperature environment (Johnston et al. 2018). However, these and other climate studies have often used the "dry" RO retrieval and focused on temperature in the UTLS region. Our focus here is to assess the quality of C1 moisture retrievals and identify the interannual water vapor variability throughout the troposphere. Because ENSO dominates tropospheric variability, we isolate and quantify the ENSO signal as part of the data validation.

In this study, we use C1 GNSS-RO observations to quantify interannual tropospheric moisture and temperature variability throughout the tropics and extratropics and to analyze how ENSO impacts this variability. The main goals of this paper are to evaluate the zonal mean specific humidity and temperature variability over 2007–18 as part of C1 data validation and quantify large-scale changes associated with ENSO from the tropics into the midlatitudes. We also assess ENSO variability in a free-running global climate model (WACCM) simulation forced with observed (historical) SSTs, in order to evaluate model ENSO variability compared to the C1 observations. Finally, we evaluate the spatial variability during several El Niño and La Niña case studies, highlighting local moisture anomalies and their correlation with changes in precipitation.

The structure of the paper is as follows: section 2 provides background on the C1, WACCM, and ERA5 data and methodology used in the study; section 3 provides a description of the C1 "wetPf2" one-dimensional variational retrieval and a comparison with the ERA5 a priori used in the C1 retrieval; section 4 presents the key results of the study, including moisture/temperature anomaly magnitude time series, linear regressions between ENSO and C1/WACCM moisture/temperature, and case studies for El Niño and La Niña events; finally, the main conclusions and future work are provided in section 5.

2. Data and analyses

a. *COSMIC-1 GNSS radio occultation*

By measuring the phase delay of radio waves from GNSS satellites as they bend through Earth's atmosphere, profiles of bending angles and refractivity can be obtained (Anthes

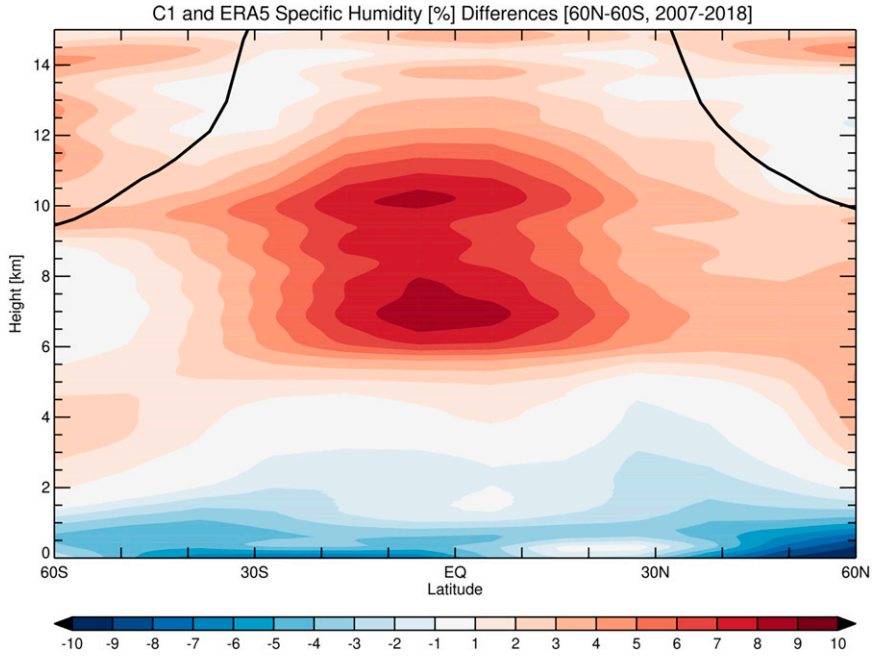

FIG. 3. Time-average zonal mean differences in specific humidity (%) between C1 and ERA5 over 2007–18. Tropopause heights are denoted by the solid black line.

2011). At microwave frequencies in the troposphere and stratosphere, the refractivity varies due to contributions from the dry neutral atmosphere and water vapor. Specifically, the atmospheric refractivity N can be related to atmospheric pressure P, temperature T, and water vapor partial pressure e (Smith and Weintraub 1953):

$$N = 77.6\left(\frac{P}{T}\right) + 3.73 \times 10^5\left(\frac{e}{T^2}\right). \quad (1)$$

In this study, C1 GNSS-RO soundings are obtained from 2007 to 2018. The C1 constellation provided up to 2500 soundings per day shortly after launch in January 2007. However, as individual satellites within the constellation went offline throughout the study period, the number of daily soundings decreased to ~250 per day at the end of 2018. We obtained the "cosmic2021" reprocessed level-2 profiles from the COSMIC Data Analysis and Archive Center (CDAAC) at the University Corporation for Atmospheric Research (UCAR). We use the new "wetPf2" retrieval, which provides refractivity, temperature, and moisture from near the surface to ~60 km. The wetPf2 product was designed to improve upon the older "wetPrf" retrieval by using a variational regularization on the Abel inversion during the retrieval process, which constrains retrievals with the aid of prior information (Wee 2018). The vertical resolution of RO soundings varies from ~200 m in the lower troposphere to ~500 m in the upper troposphere (Zeng et al. 2019) while the horizontal footprint (horizontal scale represented by a single observation; Boukabara et al. 2021) is ~200 km (Anthes et al. 2008). The retrieved profiles are reported as a function of geometric height above mean sea level and the profiles are quality controlled by excluding profiles with "bad" flags (such as if the observation bending angles exceed the climatology by a specific threshold).

Figure 1 shows the C1 zonal mean monthly sampling density during the study period using 10° latitude bands. Owing to the 72° orbital inclination of the C1 constellation, sampling is slightly lower in the tropics and highest in the midlatitudes. Sampling is largest earlier in the C1 lifespan (up to 6000 profiles in the midlatitudes from 2007 to 2010) and then steadily decreases over the years (less than 500 profiles in the tropics in 2018) due to loss of individual satellites within the constellation.

b. *Whole Atmosphere Community Climate Model*

We analyze moisture and temperature profiles from simulations using the Whole Atmosphere Community Climate Model version 6 (WACCM6). The model results analyzed here are free-running simulations of the recent past (1950–2018), which include forcings from observed SSTs, greenhouse gases, and ozone-depleting substances. Using observed SSTs forces the model to have ENSO events that are similarly timed to observations, and our objective is to compare the moisture and temperature responses in such an idealized model with the observations. The horizontal resolution of the model is 0.95° latitude × 1.25° longitude and there are 70 vertical levels (Gettelman et al. 2019) from Earth's surface to 140 km (Smith et al. 2020). We focus on simulations from 2007 to 2018 to overlap with the C1 data and zonal monthly mean analyses are shown in this study.

c. *ERA5*

ERA5 is the fifth generation of atmospheric reanalysis to be produced by the European Centre for Medium-Range Weather Forecasts (ECMWF). ERA5 provides an enhanced

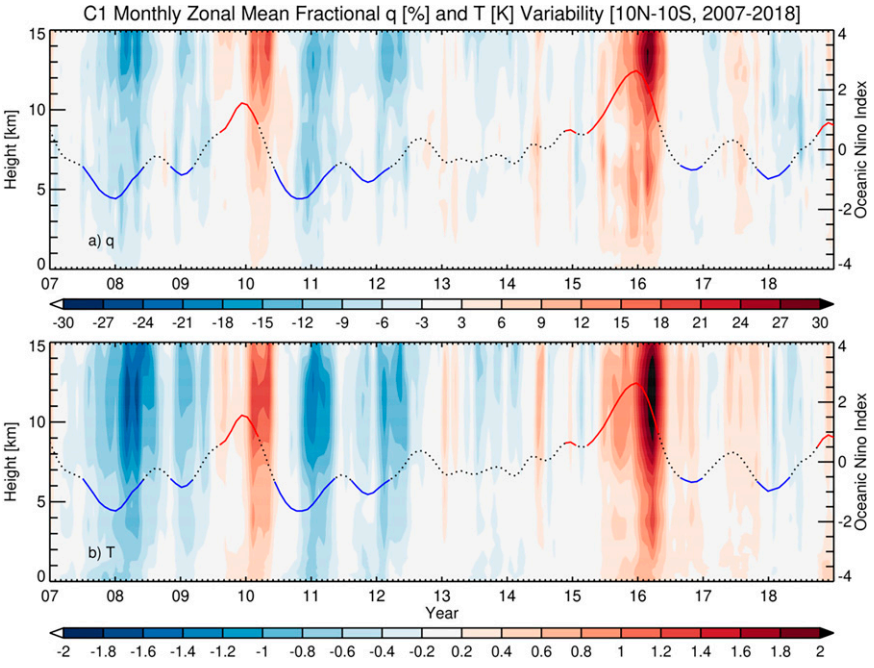

FIG. 4. Time–height cross sections of C1 monthly zonal mean (a) fractional specific humidity (%) and (b) temperature (K) variability from 2007 to 2018 within 10°N–10°S. The ONI is also shown, with the solid red line indicating El Niño events and the solid blue line indicating La Niña events.

number of output parameters over the outgoing ERA-Interim with hourly temporal resolution, a horizontal resolution of 31 km, and a vertical resolution of 37 pressure levels from 1000 to 1 hPa (Hersbach et al. 2020). Note that ERA5 assimilates COSMIC-1 bending angles. In this study, ERA5 temperature and specific humidity profiles are obtained for a comparison with the C1 wetPf2 retrievals.

d. Oceanic Niño index

The intensity of ENSO events can be characterized by several well-known tropical Pacific SST indices. In this study, we use Oceanic Niño Index (ONI) data obtained from the NOAA Climate Prediction Center from 2007 to 2018. The ONI is calculated using a 3-month running mean of sea surface temperature anomalies [using the Extended Reconstructed Sea Surface Temperature version 5 (ERSST.v5) dataset] in the Niño-3.4 region (5°N–5°S, 120°–170°W), based on centered 30-yr base periods updated every 5 years (NOAA Climate Prediction Center 2021). El Niño or La Niña occurrences are determined when a threshold of ±0.5°C is met for a minimum of 5 consecutive overlapping seasons.

e. Outgoing longwave radiation

Monthly mean outgoing longwave radiation (OLR) data are obtained from the NOAA Climate Prediction Center from 2007 to 2018 and is used to identify convection anomalies. OLR has been used in many past studies as a proxy for deep convection in the tropics (Massie et al. 2002; Randel and Park 2006; Pearson et al. 2010; Zhang et al. 2017), with lower mean OLR values (in W m^{-2}) indicating more frequently occurring deep convection (and vice versa). OLR (top of the atmosphere) is observed from the AVHRR instrument aboard the NOAA polar-orbiting spacecraft—specifically, from the *NOAA-18* satellite during this study period. This is an interpolated dataset, which is done to fill in gaps in the data and minimizes the distance in space and time over which a value is interpolated (Liebmann and Smith 1996). The data are provided on a 2.5° × 2.5° latitude–longitude grid.

f. Methodology

C1 and WACCM moisture and temperature profiles are obtained between 60°N and 60°S from 2007 to 2018 using a height range of nearest to surface to 20 km. Each C1 and WACCM profile is interpolated to a 50-m uniform vertical grid using a quadratic interpolation scheme and then smoothed to 250 m, which is roughly the native resolution for RO profiles in the troposphere. First, zonal mean variability is analyzed using both time–height and time–latitude diagrams. To derive interannual variations in the moisture and temperature fields, specific humidity (q) and temperature (T) profiles are binned by month and the 12-yr monthly mean is then removed. Also, spatial variability (using 5° latitude × 10° longitude gridding) at various altitudes is shown during different El Niño and La Niña seasons to highlight key moisture and temperature changes that occur between these events and relate these changes to fluctuations in deep convection. For this analysis, q and T profiles are binned by season [e.g., January–March (JFM)] and the 12-yr seasonal mean is also removed. JFM is chosen for

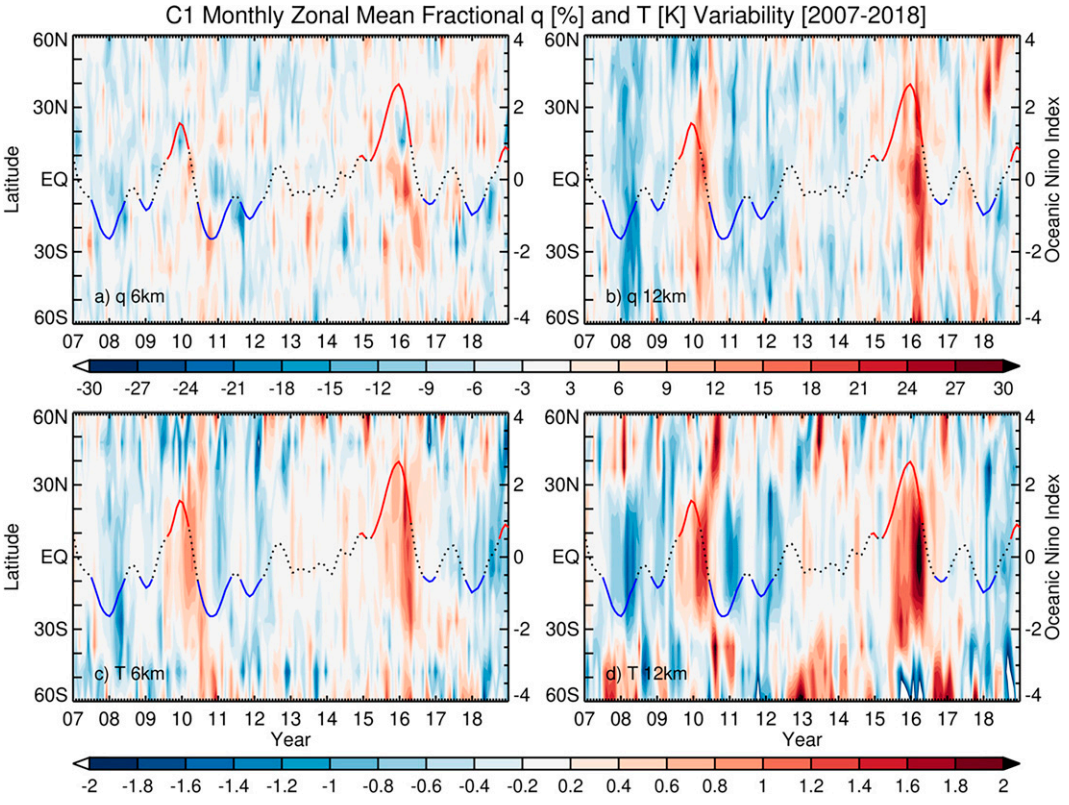

FIG. 5. Time–latitude cross sections of C1 monthly zonal mean (top) fractional specific humidity (%) and (bottom) temperature (K) variability from 2007 to 2018 at (a),(c) 6 and (b),(d) 12 km. The ONI is also shown, as in Fig. 4.

study to account for the 2–3-month lag in tropospheric q and T anomalies in responding to the November/December peak of SST anomalies, and this lag will be discussed later in the manuscript.

3. C1 1D-Var retrieval

The UCAR CDAAC wetPf2 one-dimensional variational (1D-Var) retrieval uses an a priori state of the atmosphere (background vertical profile), an observable (RO refractivity or bending angle), and their specified associated errors to retrieve best-fit temperature and moisture profiles that minimize a quadratic cost function (Rieckh et al. 2018). ERA5 pressure-level temperature and humidity profiles are used as the a priori, which are interpolated to the time and location of the occultation. Figure 2 shows the contribution of the dry neutral atmosphere and water vapor terms in the refractivity equation, Eq. (1), to the overall refractivity profile over the Pacific warm pool (a region with considerable atmospheric moisture) and globally, as well as how this impacts the retrieved temperature and dry temperature profiles. Refractivity decreases exponentially with height in the troposphere. Within the boundary layer (~0–2 km), where moisture amounts are largest, the water vapor term (N_{wet}) can account for 25%–30% of the observed refractivity. However, the dry neutral atmosphere term (N_{dry}) still contributes the most to refractivity in the troposphere and contributes nearly 100% above ~12 km since moisture is generally negligible above this altitude (Figs. 2a,c). This can also be seen in the differences between T and T_{dry} (Fig. 2b), as $T - T_{\text{dry}}$ can be over 80 K near the surface while differences are nearly zero above 12 km. Thus, at high altitudes, the refractivity due to water vapor is too small to be detected by GNSS-RO and wetPf2 moisture retrievals shown at these altitudes mainly contain information from the a priori (ERA5) rather than observational information.

While the C1 1D-Var retrieval uses ERA5 as an a priori to derive moisture and temperature profiles, this does not mean that C1 q and T profiles are identical to ERA5. Figure 3 shows the time-average zonal mean q differences between C1 and ERA5 between 60°N and 60°S. As is well known, negative RO refractivity bias occurs within the boundary layer (<2 km) due to a combination of various receiver tracking errors and the presence of superrefraction (Rocken et al. 1997; Ao et al. 2003; Yu et al. 2018; Feng et al. 2020), which results in relatively large negative q biases for RO at these altitudes. Above the boundary layer, minor differences are observed within ~2–5 km, while C1 displays a positive bias of 6%–8% in the tropical middle troposphere. These results are similar to biases between COSMIC-2 and ERA5 shown in Johnston et al. (2021). Since reanalysis assimilation systems often rely on moisture data sources that have larger uncertainties in the presence of deep tropical clouds, the larger differences observed in the tropical midtroposphere may be due

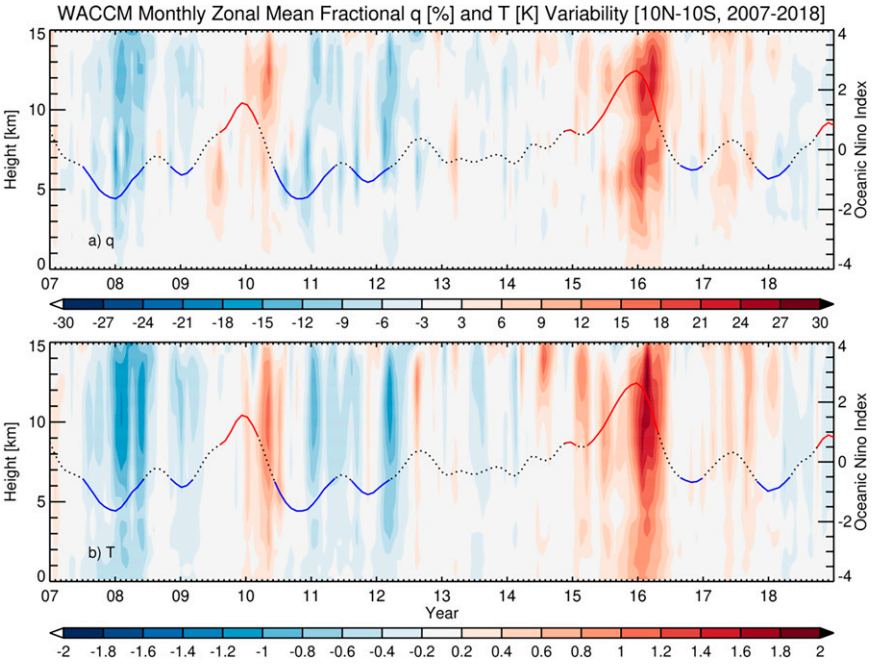

FIG. 6. Time–height cross sections of WACCM monthly zonal mean (a) fractional specific humidity (%) and (b) temperature (K) variability from 2007 to 2018 within 10°N–10°S. The ONI is also shown, as in Fig. 4.

to ERA5 underestimating the moisture. Previous studies have revealed that reanalysis mid-to-upper-tropospheric humidity is slightly dry in regions associated with deep convection and have suggested that this could be due to insufficient model convective parameterization (Luo et al. 2008; Takahashi et al. 2016; Xue et al. 2020). Thus, the C1 1D-Var retrievals may provide significant added value in these regions. C1 and ERA5 agreed well in temperature throughout the troposphere above the boundary layer (not shown), with C1 showing a small positive bias up to 0.2 K in the middle troposphere and differences < 0.1 K elsewhere. Along with the mean biases, we also evaluated the correlations between monthly zonal mean q variations from C1 and ERA5 (not shown). The correlations were extremely high (>0.9) over all latitudes throughout the troposphere, demonstrating strong similarity between C1 and ERA5 for monthly zonal mean variability. This may be partly due to the fact that monthly zonal mean q variations typically have broad spatial and vertical scales that are well resolved in both datasets.

Finally, it is important to understand the dependence of the 1D-Var retrieval on the a priori. This dependence was evaluated in the tropics by deriving another C1 wetPf2 dataset for one month using the National Centers for Environmental Protection (NCEP) Global Forecast System (GFS) operational analysis as the a priori (instead of ERA5) and comparing the q and T differences between the two C1 1D-Var retrievals to the differences between their corresponding a priori (see Fig. 1 in the online supplemental material). In this comparison, the mean differences between the C1 retrievals were smaller relative to the corresponding a priori mean differences for q within the lower/middle troposphere and for T within the UTLS, while the standard deviation of the differences was considerably reduced for the C1 retrievals relative to the a priori at the same altitudes. These smaller mean differences and standard deviations demonstrate that the C1 1D-Var has more independence from its a priori for q and T within the lower/middle troposphere and UTLS, respectively. In contrast, the mean differences between the C1 retrievals displayed similar patterns and magnitudes to the corresponding a priori mean differences for q within the upper troposphere and for T within the lower/middle troposphere, while the standard deviation of the differences was only slightly reduced for the C1 retrievals at these altitudes, indicating that the C1 1D-Var has a stronger dependence on its a priori for q and T within the upper troposphere and lower/middle troposphere, respectively.

4. Results

a. C1 zonal mean variability

The C1 zonal mean tropospheric fractional specific humidity and temperature variability in the deep tropics (10°N–10°S) from 2007 to 2018 are shown in time–height cross sections in Fig. 4, with the ONI overplotted to highlight the role that ENSO plays in forcing the observed atmospheric variability. Both the observed q and T variability show a clear relationship with ENSO, as large increases in tropospheric q and T are seen during El Niño events while decreases are observed during La Niña events. The q anomalies in the lower

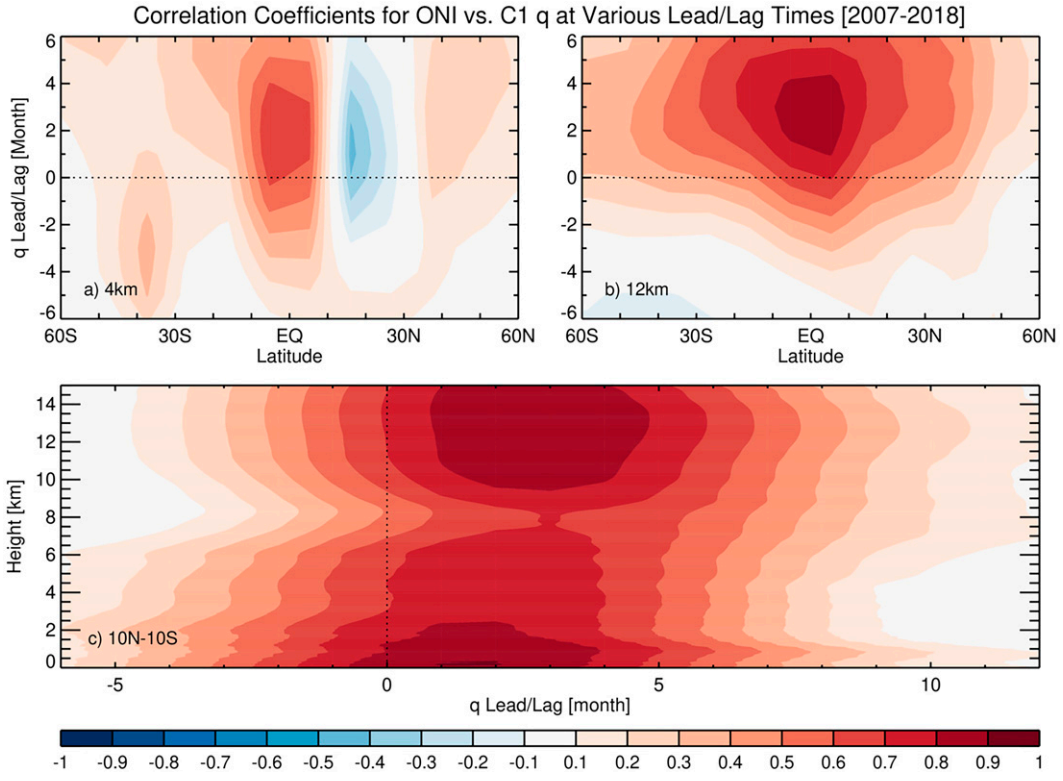

FIG. 7. Correlation coefficients between the Oceanic Niño Index (ONI) vs C1 q at various lead and lag times and latitudes at (a) 4 and (b) 12 km, as well as (c) for various lead and lag times and heights within 10°N–10°S.

troposphere are generally within ±15% and increase in magnitude into the upper troposphere (up to ±30%). Anomaly patterns are similar for T; again, anomaly magnitudes increase from the lower troposphere (within ±1 K) into the upper troposphere (within ±2 K). This behavior is consistent with a temperature response to SST anomalies by a moist adiabatic relationship (Santer et al. 2005). Anomaly magnitudes are strongly influenced by the strength of the SST anomalies, as the largest increases in q and T occur during the robust El Niño of 2015/16 and the largest decreases are observed during the La Niña of 2007/08.

Next, we show the observed q and T variability using time–latitude cross sections in the middle and upper troposphere in Fig. 5 to resolve whether the ENSO-forced variability is limited to the tropics or also occurs into the extratropics. For q at 6 km (Fig. 5a), anomalies consistent with the ENSO signal [moisture increases (decreases) during El Niño (La Niña)] are generally restricted to within the deep tropics and are in the range ±15%. Beyond those latitudes, considerable noise is apparent as the q variability is impacted by a variety of other factors. At 12 km (Fig. 5b), the q anomalies show remarkable consistency with ENSO even into the midlatitudes and again increase in magnitude, similar to Fig. 4. For example, increases in moisture of up to 20%–30% are evident during the El Niño events of 2009/10 and 2015/16 from ~40°N to 60°S, while the strong La Niña of 2007/08 produced moisture decreases of 20%–30% throughout the entire study region. In contrast, coherency of the zonal mean T anomalies with ENSO is generally observed within 30°N–30°S at both 6 and 12 km (Figs. 5c,d). The largest magnitudes are usually observed within 10°N–10°S, ranging from ±1 K at 6 km and ±2 K at 12 km. This zonal mean warming of the tropical and subtropical troposphere is a well-known feature of ENSO and agrees well with previous studies (Yulaeva and Wallace 1994; Calvo Fernández et al. 2004; Scherllin-Pirscher et al. 2012; Randel and Wu 2015). As a note, we also conducted similar analyses to Figs. 4 and 5 using the ERA5 pressure-level data (not shown), which displayed extremely similar q and T variability patterns and magnitudes to C1. Additionally, previous studies (e.g., Johnston et al. 2021) have shown close agreement between GNSS-RO and ERA5 tropospheric moisture. This excellent agreement further attests to the capability of using GNSS-RO 1D-Var retrievals for climate studies.

b. *WACCM zonal mean variability comparison*

We analyze the zonal mean q and T variability within WACCM to evaluate the response to observed SST forcing in a free-running climate model. We focus on the WACCM time–height diagram of zonal mean tropospheric fractional specific humidity and temperature variability from 2007 to 2018 in Fig. 6. Within 10°N–10°S, the tropospheric q and T variability show comparable patterns to the C1 observations (Fig. 4), with q and T increases (decreases) during El Niño (La Niña). A key difference evident is that WACCM anomaly

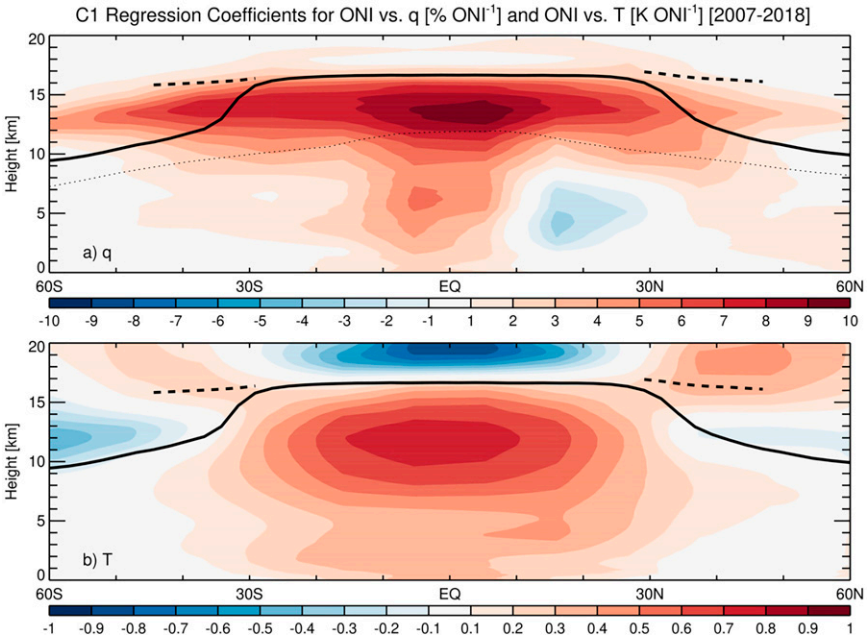

FIG. 8. Latitude–height cross sections of regression coefficients between the Oceanic Niño Index (ONI) and zonal mean C1 (a) specific humidity and (b) temperature. Units are % per normalized ONI for specific humidity and K per normalized ONI for temperature. Regression coefficients are calculated with the ONI time series leading by 2 months. Tropopause heights are denoted by the solid black line and double tropopause heights are denoted by the dashed black line. The thin dotted line in (a) indicates the top of the colored contours from Fig. 2c and is approximately the level at which the moisture information content is almost exclusively from the a priori.

magnitudes are somewhat smaller than C1 at most altitudes during the major ENSO events in the study period, with WACCM q variability often ±6% smaller while T variability is often ±0.4 K smaller. This feature is especially noticeable during the shorter-duration 2009/10 El Niño event, as WACCM q and T anomaly magnitudes are relatively small and less well defined. However, in spite of this difference, these results show there is generally good agreement between C1 and WACCM in identifying ENSO-forced q and T variability throughout the troposphere.

c. *Isolating ENSO behavior from regressions*

In this section, we perform a standard linear regression to isolate the relationship between the ONI and zonal mean q and T in both C1 and WACCM. Figure 7 shows the correlation coefficients for ONI versus C1 q for various lead and lag times and latitudes at 4 and 12 km, as well as for tropospheric heights within 10°N–10°S. In the lower troposphere, the strongest correlations occur in the deep tropics (±10°). However, in the upper troposphere, correlations become stronger (R values up to 0.9 at 12 km) and expand into the subtropics and midlatitudes. The correlation patterns suggest two distinct regions of q response to ENSO, with the first region within the lower to midtroposphere (10°N–10°S, up to ~8 km) highlighted by a peak q lag time of 2 months while the second region is within the upper troposphere (~50°N–50°S, ~8–15 km) with a peak q lag time of 2–3 months. The lagged response for the zonal mean q can be attributed to exchange of fluxes at the atmosphere–ocean interface and the atmospheric energy loss to space and to the midlatitudes (Su et al. 2005; Scherllin-Pirscher et al. 2012). While ONI correlations with T are not shown here, a 2–3-month T lag also produced the strongest correlations, which is consistent with previous studies (e.g., Randel and Wu 2015).

The near-global structure of regression coefficients between the ONI and C1/WACCM q and T are shown in Fig. 8, using a 2-month time lag for both q and T. While the C1 q retrievals in the tropics primarily contain information from RO measurements below ~12 km (as discussed above), we include results up to 20 km in Fig. 8 to highlight ENSO structure to tropopause altitudes; q results above ~12 km are closely tied to the ERA5 a priori. The q variations (Fig. 8a) are expressed in terms of local percentage variations per ONI (hereafter X% ONI^{-1}, with an analogous format for temperature), and the patterns highlight distinct variability in the lower and upper troposphere. The positive signal observed for lower-tropospheric q over 10°N–10°S is mostly related to collocated enhancements of convection (as shown below), and the out-of-phase negative signal near 15°–20°N is consistent with ENSO strengthening of the downwelling branch of the Hadley circulation (Seager et al. 2003). Fractional moisture anomalies are small in the tropical lower troposphere (~2%–3% ONI^{-1}) and increase with height into the middle troposphere. In the

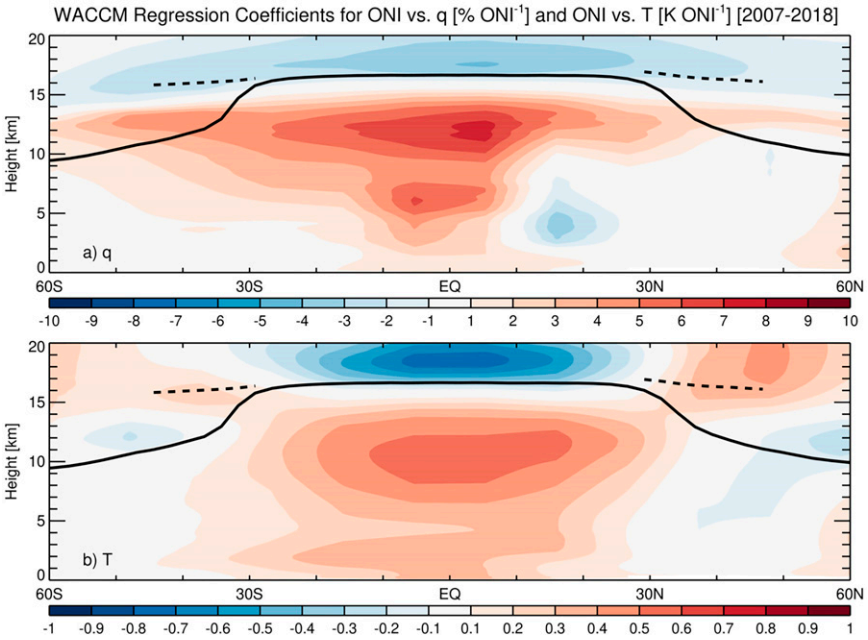

FIG. 9. Latitude–height cross sections of regression coefficients between the Oceanic Niño Index (ONI) and zonal mean WACCM (a) specific humidity and (b) temperature. Units are % per normalized ONI for specific humidity and K per normalized ONI for temperature. Regression coefficients are calculated with the ONI time series leading by 2 months. Tropopause heights are denoted by the solid black line and double tropopause heights are denoted by the dashed black line.

upper troposphere, the positive signal becomes much stronger (up to 10% ONI^{-1}) and expands broadly in latitude into the subtropical upper troposphere and across the tropopause into the midlatitude lower stratosphere of both hemispheres. The mechanism for the meridional expansion of the moisture anomalies into the midlatitude lower stratosphere remains unclear and would merit further study.

A strong positive ENSO signal is evident for zonal mean T within 30°N–30°S throughout the troposphere (Fig. 8b), which is a well-known feature from previous results (e.g., Seager et al. 2003; Scherllin-Pirscher et al. 2012). The positive ENSO T response is nearly spatially uniform between about 20°N and 20°S, associated with weak horizontal temperature gradients (Seager et al. 2003). Note that T anomalies increase from the lower troposphere (~0.3 K ONI^{-1}) into the upper troposphere (~0.8 K ONI^{-1}), and this vertical structure is consistent with a moist adiabatic temperature response (see Fig. 2 in the online supplemental material). In the tropical lower stratosphere, a thin layer of cooling occurs during an El Niño event (up to −0.9 K ONI^{-1}), which has been shown in prior studies (e.g., Randel et al. 2009; Free and Seidel 2009) and is related to stronger ENSO-induced upwelling near the tropical tropopause (Randel et al. 2009).

Corresponding ENSO variations for the WACCM q and T fields are shown in Fig. 9. Spatial patterns in WACCM q and T anomalies due to ENSO are similar to the observations, including latitudinal spreading of the q anomalies above ~8 km and the negative q maxima in the NH subtropics. Magnitudes are similar for the C1 and WACCM q and T anomalies from the surface up to the middle troposphere, while WACCM shows smaller anomalies in the upper troposphere. Additionally, the WACCM upper-tropospheric q and T patterns do not reach all the way to the tropical tropopause but fall off above ~14 km. There are negative moisture anomalies seen within the lower stratosphere for WACCM which are likely caused by the negative WACCM T anomalies at the tropical cold-point tropopause (CPT), as the tropical CPT is an important determinant for water vapor transport to the stratosphere (Pan et al. 2018). This behavior is not seen in the C1 results (Fig. 8), where there is a very small ENSO influence on the CPT.

d. *El Niño and La Niña case studies*

We include case studies of El Niño and La Niña events to identify the spatial variability of tropospheric moisture and temperature during each event, quantify major differences between events, and relate regions with considerable increases/decreases in moisture to changes in deep convection. For reference, Fig. 10 shows the boreal winter seasonal mean q (during January–March) at 6 km along with the mean OLR (as a proxy for deep convection). The regions with the largest amounts of moisture occur in the tropics and are concentrated in three major areas: the Pacific warm pool/Maritime Continent, central Africa, and northern South America. These regions match up particularly well with OLR minimums, as

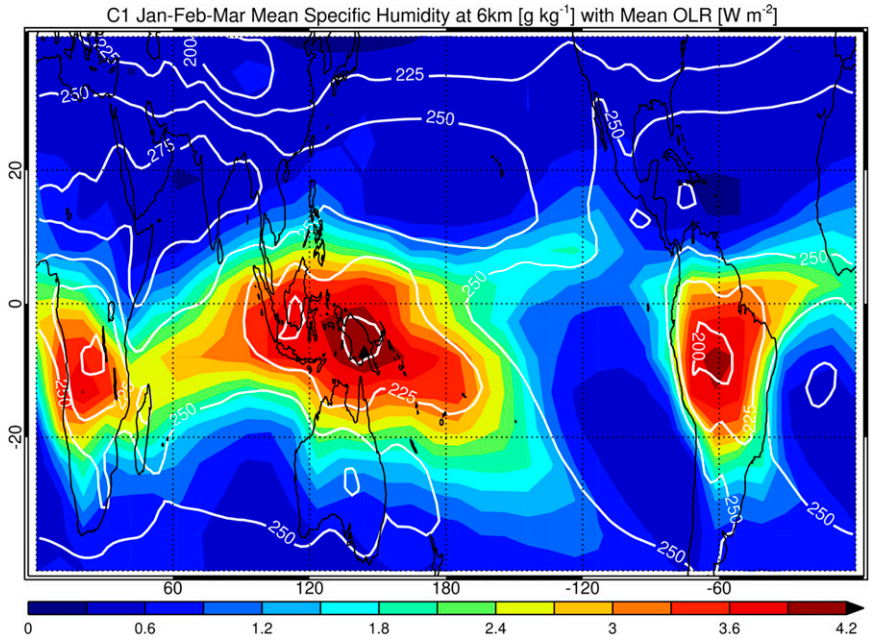

FIG. 10. C1 seasonal (JFM) mean specific humidity (g kg^{-1}; color contours) at 6 km and outgoing longwave radiation (W m^{-2}; solid white contours) within 40°N–40°S from 2007 to 2018.

mean OLR values < 200 W m^{-2} are often observed in the centers of these regions with the highest moisture.

During late 2009 into early 2010, the tropical Pacific Ocean was dominated by an El Niño event that exhibited record-breaking warm SST anomalies in the central Pacific, which is in contrast to the more commonly known eastern Pacific El Niño events. Termed El Niño Modoki or central Pacific (CP) El Niño, these events have been occurring more frequently in recent decades (Kim et al. 2011). The generation mechanism of El Niño CP involves the zonal advective feedback and forcing from the subtropical atmosphere (Kug et al. 2009; Yu and Kim 2010; Capotondi 2013; Paek et al. 2017). The important changes to q, T, and OLR that can occur during ENSO CP events are shown in Fig. 11 during JFM 2010 at 6 and 12 km. The q at 6 km (Fig. 11a) shows large positive anomalies (50%–80%) over the equatorial central Pacific, and this increase in moisture continues east and northeastward across the North Atlantic toward southern Europe. These impacts propagate into the winter hemisphere midlatitudes more efficiently because of relatively stronger seasonal subtropical and subpolar jet streams (Ashok et al. 2007). There are also many regions where considerable moisture decreases are observed (40%–70%), such as near and east of Hawaii, over the African Sahel region, and over the western Pacific. Regions with large increases (decreases) in q are correlated well with large decreases (increases) in OLR. For example, OLR anomalies of over -30 W m^{-2} are observed over the central Pacific and this again extends northeastward across the North Atlantic. At 12 km (Fig. 11b), q increases are again observed over many of the same regions as at 6 km, although anomaly magnitudes are slightly weaker in general. However, there are now many additional regions with more moderate moisture increases (10%–40%), such as over much of the Southern Hemisphere subtropics and midlatitudes. Temperature increases are observed across the majority of the tropics (Figs. 11c,d) with the largest anomaly magnitudes seen over the eastern Pacific. However, the T anomalies are not well correlated with OLR anomalies, as there is a "dumbbell"-shaped pattern in the T anomalies that straddles the equator over the eastern Pacific. These twin peaks in the T anomalies correspond to the positions of the anticyclonic gyres at the jet stream level, flanking the region of enhanced precipitation that develops over the central Pacific near and to the east of the date line during El Niño events (Yulaeva and Wallace 1994). The T increases are generally up to 2 K at 6 km, while at 12 km T increases to between 3 and 4 K and expands into the Northern Hemisphere midlatitudes.

The 2015/16 ENSO event is typically considered one of the top three strongest El Niño events in the historical record dating back to 1950, with maximum SST anomalies reaching ~3.5°C. This event is considered to be a hybrid of the previously described El Niño CP and the more conventional eastern Pacific (EP) El Niño (Paek et al. 2017). The EP El Niño is generated by SST anomalies forming in the equatorial eastern Pacific due to weakening of the Pacific Walker circulation and the southeasterly trade winds (Wyrtki 1975). However, this event differed from previous major El Niño events in that the west-central Pacific subsurface and surface temperature anomalies were much warmer, the eastern Pacific was comparatively cooler, and the trade winds were weaker (L'Heureux et al. 2017). Figure 12 shows the seasonal mean q, T, and OLR anomalies during JFM 2016 (shortly after the maximum in

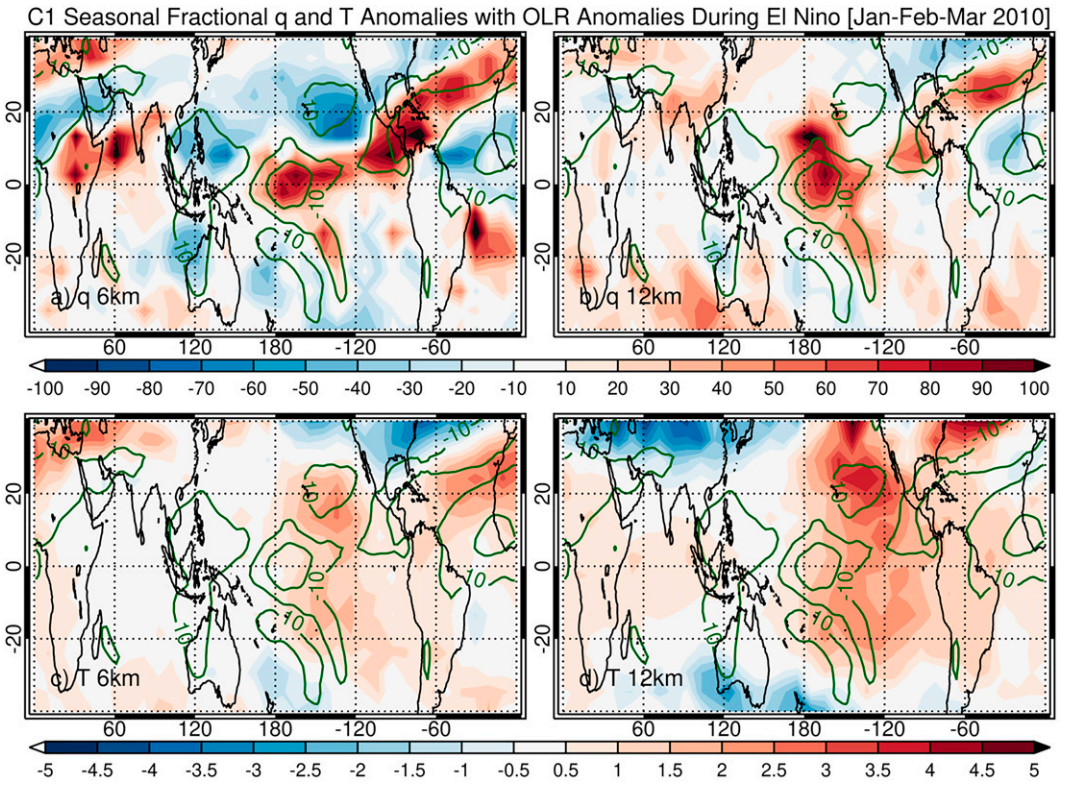

FIG. 11. C1 seasonal mean (JFM 2010) (top) fractional specific humidity (%) and (bottom) temperature (K) anomalies at (a),(c) 6 and (b),(d) 12 km for the 2009/10 El Niño event. Seasonal mean OLR anomalies (W m^{-2}) are also shown with the solid green contours.

SST anomalies) at 6 and 12 km. The q at 6 km (Fig. 12a) shows much larger increases in moisture (>100%) over much of the equatorial central and eastern Pacific relative to JFM 2010, and this increase extends toward the coasts of western South America and Central America. However, the subtropical and subpolar jets are not as strong relative to JFM 2010, resulting in more moderate moisture increases across the North Atlantic into southern Europe. Considerable q decreases (40%–70%) are also observed in many similar locations as JFM 2010. Regions experiencing large q anomalies are again well correlated with changes in OLR and precipitation, especially over the central/eastern Pacific, where OLR decreases of more than 50 W m^{-2} are observed. A linear regression was conducted for the gridded q and OLR anomalies for each case study (not shown). Correlations for each event range from −0.55 to −0.6 between 40°N and 40°S and increase between 20°N and 20°S (ranging from −0.7 to −0.8). At 12 km (Fig. 12b), the q anomaly characteristics are similar to JFM 2010, as many additional regions display moderate moisture increases (10%–40%), including much of the subtropics and midlatitudes, while most of the regions that experienced large q decreases at 6 km see moisture values closer to normal at 12 km. Considerable T increases are observed across the majority of the tropics at both 6 and 12 km (Figs. 12c,d), with the largest anomaly magnitudes seen over the eastern Pacific in the same dumbbell-shaped pattern. However, the eastern Pacific anomaly magnitude is now much larger at both altitudes, with positive anomalies ranging from 2 to 3 K at 6 km and rising to 4–5 K at 12 km. Additionally, T increases throughout the rest of the tropics are much larger for this event. For example, during JFM 2010, positive anomalies were generally <1 K at both altitudes while during JFM 2016, T increases of up to 2.5 K are observed, confirming that larger Pacific Ocean SST anomalies also produce larger atmospheric T anomalies across the entirety of the tropics.

The previously described 2009/10 El Niño event quickly dissipated in early 2010 and went through the fastest phase transition to a La Niña event among all other CP El Niño events (Kim et al. 2011). This 2010/11 event produced many global climate impacts, including some of the worst floods in modern Australian history (Semenov et al. 2012). La Niña conditions declined into early 2011 and then restrengthened and continued into early 2012. This is known as a "double-dipping" La Niña, which can occur when eastward propagating downwelling warm equatorial Kelvin waves occur during the decaying phase of the first La Niña (Zheng et al. 2015). The seasonal mean q, T, and OLR anomalies are shown in Fig. 13 during JFM 2011 at 6 and 12 km. The q at 6 km and 12 km (Figs. 13a and b) shows large decreases in moisture (40%–50%) in the equatorial central Pacific, centered along the international date line, and extending southeastward due to a weaker-than-normal South Pacific convergence zone

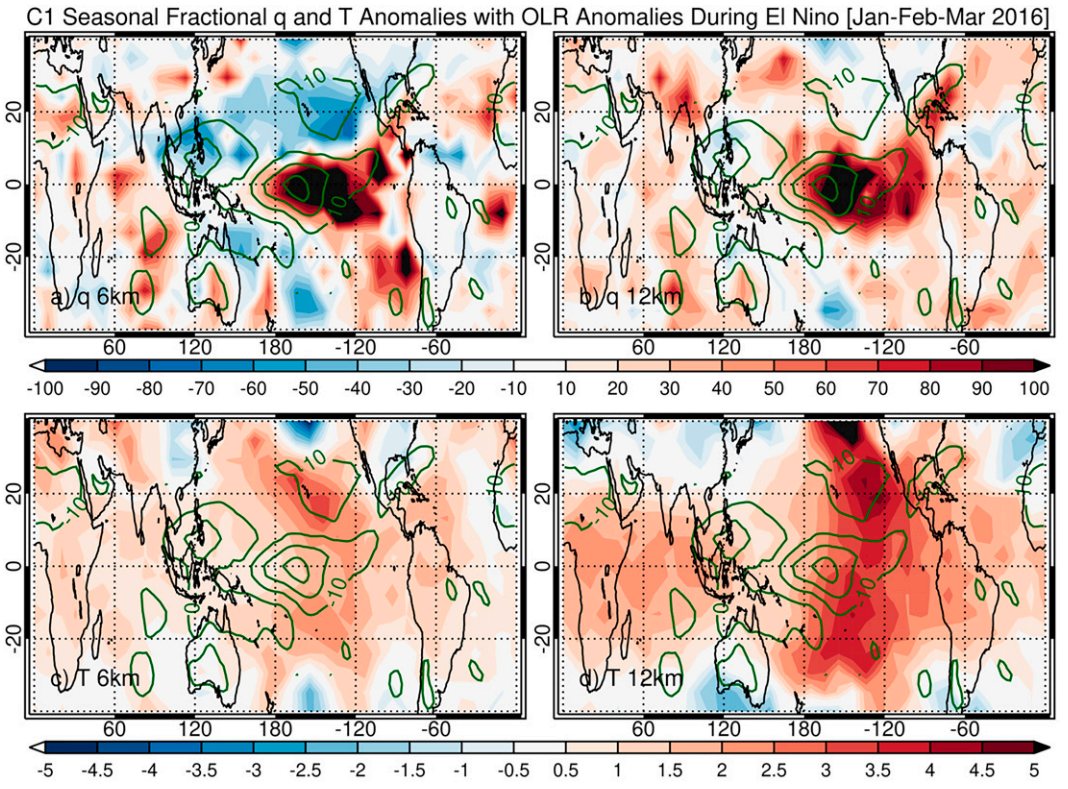

FIG. 12. C1 seasonal mean (JFM 2016) (top) fractional specific humidity (%) and (bottom) temperature (K) anomalies at (a),(c) 6 and (b),(d) 12 km for the 2015/16 El Niño event. Seasonal mean OLR anomalies (W m^{-2}) are also shown with the solid green contours.

(SPCZ). This region of decreased moisture also has positive OLR anomalies and decreased precipitation. Additional regions experiencing moisture decreases include Central America, the southeastern United States, and east-central Africa. In contrast, extraordinary increases in midlevel q are observed over northern Australia (50%–70%), Southeast Asia (>100%), and into the North Pacific nearly to Hawaii (50%–70%), with many of these locations also experiencing corresponding OLR decreases of more than 30 W m^{-2} and increases in precipitation. Interestingly, many of these moisture hotspots display milder upper-level q increases. Similar to El Niño events, T anomalies for La Niña do not correlate well with OLR anomalies. Notably, T decreases are observed at both 6 and 12 km (Figs. 13c and 13d) throughout the majority of the tropics. The largest anomaly magnitude is observed in the eastern Pacific in the familiar dumbbell-shaped pattern, with T decreases of 1.5–2 K at 6 km becoming larger (3–4 K) at 12 km.

In summary, these case studies show that, in general, large increases (decreases) in moisture are often accompanied by large increases (decreases) in deep convection as well. These changes typically occur on a more regional scale, whereas temperature variability occurs on a much larger scale (e.g., throughout the entire tropics). We also demonstrated that many regional differences can occur for q and OLR anomaly locations/magnitudes for the two types of El Niño events (the 2009/10 CP El Niño and the CP/EP hybrid of 2015/16), highlighting the need for continued research on the differences between these events.

5. Conclusions

In this paper, the interannual variability of tropospheric moisture and temperature and their relationships to ENSO were analyzed using retrievals from C1 GNSS-RO observations between 60°N and 60°S from 2007 to 2018. Time series of C1 tropical zonal mean q and T showed clear relationships with ENSO, with large increases (decreases) in tropospheric q and T observed during El Niño (La Niña) events. The q and T anomaly magnitudes were smallest in the lower troposphere (±15% and ±1 K) and increased into the upper troposphere (±30% and ±2 K). Variability was influenced by the strength of the SST anomalies, as the largest q and T anomalies occurred during the strongest El Niño and La Niña events. Linear regressions between the ONI and zonal mean q from C1 suggested two distinct regions of coherent ENSO influence. The lower/middle troposphere (<8 km) showed positive q anomalies confined to within ~10°N–10°S (2%–5% ONI^{-1}), and negative anomalies over 15°–20°N were consistent with ENSO enhancement of the downwelling branch of the Hadley circulation. Fractional moisture anomalies became larger into the tropical upper troposphere (up to 10% ONI^{-1}) and expanded broadly into the subtropical upper troposphere and across the tropopause

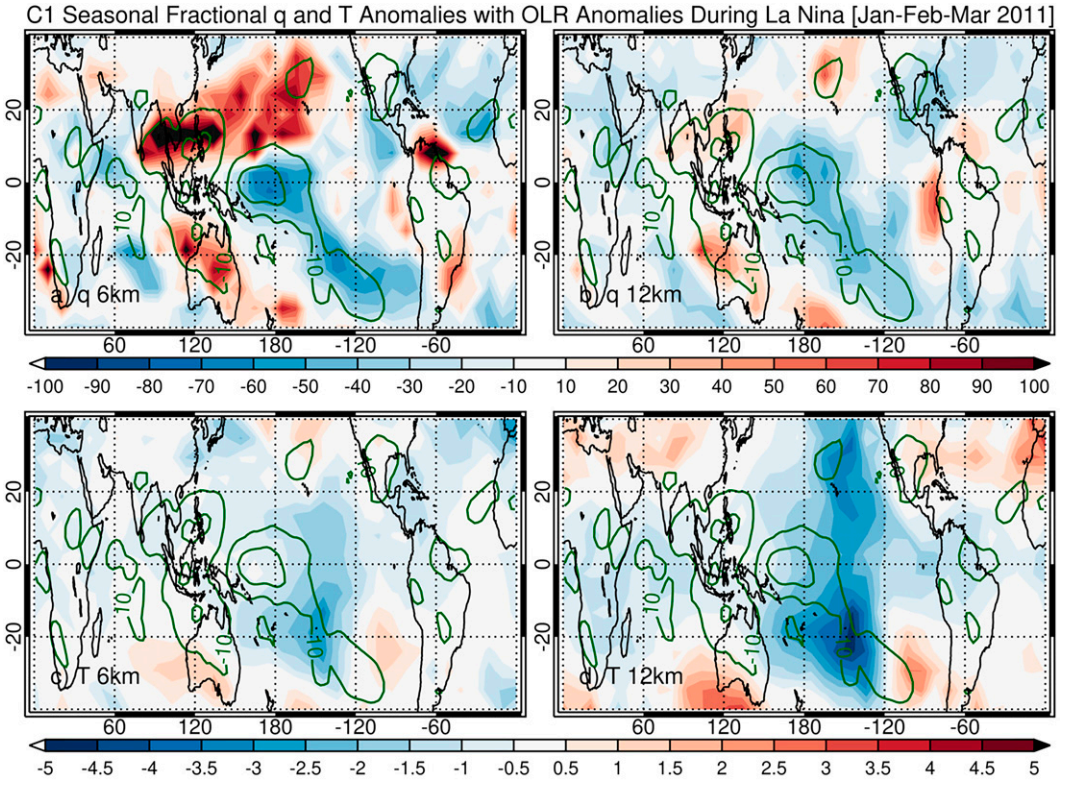

FIG. 13. C1 seasonal mean (JFM 2011) (top) fractional specific humidity (%) and (bottom) temperature (K) anomalies at (a),(c) 6 and (b),(d) 12 km for the 2010/11 La Niña event. Seasonal mean OLR anomalies (W m^{-2}) are also shown with the solid green contours.

into the midlatitude lower stratosphere. The mechanism for the meridional expansion of this strong relationship remains unclear. Positive T anomalies were observed within 30°N–30°S throughout the troposphere, increasing in magnitude from the lower-to-upper troposphere (from ~0.3 K ONI^{-1} up to 0.8 K ONI^{-1}). The tropospheric temperature vertical structure was consistent with a moist adiabatic temperature response. A thin layer of negative T anomalies was also identified in the tropical lower stratosphere, which is a well-known feature tied to ENSO-induced variations in upwelling near the tropical tropopause.

We included comparisons with a free-running WACCM simulation forced by observed SSTs to evaluate ENSO variability in an idealized model setting. In general, WACCM simulations showed comparable tropospheric zonal mean patterns to the C1 observations, indicating that the observed SST forcing within the model produces realistic interannual tropospheric variability. It is important to note that this does not necessarily validate the model output since model biases (such as insufficient convective parameterization) that influence tropospheric q and T could be common between WACCM and the ERA5 a priori, and any ERA5 biases would be partly inherited by the C1 retrievals. The key differences between the two datasets were that C1 showed a larger positive signal for both q and T throughout the upper troposphere (±6% and ±0.4 K during the major ENSO events in the study period) and negative q anomalies were evident within the lower stratosphere for WACCM.

Finally, case studies for two El Niño events and one La Niña event were used to identify the spatial variability of tropospheric q and T during each event, and to relate q anomalies to changes in regional precipitation. Many similarities and differences were observed between the two El Niño events. Large q increases were observed over the central Pacific in both events, although anomalies were considerably larger for the stronger 2015/16 hybrid EP/CP El Niño. In contrast, the 2009/10 CP El Niño produced a stronger, more persistent subtropical jet over the North Atlantic into southern Europe, bringing large moisture increases into these regions. Moisture anomalies were typically well aligned with OLR anomalies, while temperature anomalies often showed weak correlation with the collocated changes in precipitation. Large T increases were observed throughout the entire tropics for both events, especially over the eastern Pacific, and magnitudes increased considerably from 6 to 12 km. In contrast, the opposite regional impacts to both q and T were generally observed for the 2010/11 La Niña event. These case studies showed that large increases (decreases) in moisture were often accompanied by large increases (decreases) in deep convection, which typically occurred on a more regional scale, whereas coherent temperature variability occurred on a much larger scale.

Key new results shown in this study include the increase in moisture variability magnitudes from the lower troposphere into the upper troposphere, a strong relationship between ENSO and moisture into the subtropical upper troposphere and midlatitude lower stratosphere, and close agreement between regional moisture anomalies and changes in deep convection during ENSO events. There are a few caveats to be noted in this research. In addition to the limited information content of RO water vapor retrievals in the upper levels described earlier in the manuscript, C1 sampling density declined significantly throughout the study period. While this could have been partially offset by including data from other RO missions, the CDAAC wetPf2 retrieval is not yet available for most older missions and our preference was to use data with consistent processing to limit potential uncertainties from merging different datasets. Possibilities for future study include expanding the study time period since the recently launched COSMIC-2 mission provides greatly increased sampling density in the tropics and subtropics, as well as expanding upon the moisture–temperature relationship throughout the tropics.

Acknowledgments. The authors thank the COSMIC neutral atmosphere science group for many helpful discussions on this research, Rick Anthes for reviewing the manuscript, Jon Starr for help with processing the WACCM data, Teresa Vanhove for processing C1 wetPf2 data with a different a priori, and three anonymous reviewers for their valuable comments on the manuscript. This work has been supported by NSF–NASA Grant AGS-1522830 and NOAA Contract 16CN0070. We thank Eric DeWeaver (NSF) and Jack Kaye (NASA) for their long-term support of COSMIC.

Data availability statement. All data used in this study are freely and openly available. C1 data were obtained from CDAAC at UCAR (https://www.cosmic.ucar.edu/what-we-do/cosmic-1/data/). ERA5 data were obtained from ECMWF through the Copernicus Climate Change Service (https://cds.climate.copernicus.eu/#!/search?text=ERA5&type=dataset). WACCM data were obtained from UCAR (https://www.acom.ucar.edu/waccm/download.shtml). ONI data were obtained from the NOAA Climate Prediction Center (https://origin.cpc.ncep.noaa.gov/products/analysis_monitoring/ensostuff/ONI_v5.php). OLR data were obtained from the NOAA Physical Sciences Laboratory (https://psl.noaa.gov/data/gridded/data.olrcdr.interp.html).

REFERENCES

Anthes, R. A., 2011: Exploring Earth's atmosphere with radio occultation: Contributions to weather, climate and space weather. *Atmos. Meas. Tech.*, **4**, 1077–1103, https://doi.org/10.5194/amt-4-1077-2011.

——, and Coauthors, 2008: The COSMIC/FORMOSAT-3 mission: Early results. *Bull. Amer. Meteor. Soc.*, **89**, 313–333, https://doi.org/10.1175/BAMS-89-3-313.

Ao, C. O., T. K. Meehan, G. A. Hajj, A. J. Mannucci, and G. Beyerle, 2003: Lower troposphere refractivity bias in GPS occultation retrievals. *J. Geophys. Res.*, **108**, 4577, https://doi.org/10.1029/2002JD003216.

Ashok, K., S. K. Behera, S. A. Rao, H. Weng, and T. Yamagata, 2007: El Niño Modoki and its possible teleconnection. *J. Geophys. Res.*, **112**, C11007, https://doi.org/10.1029/2006JC003798.

Boukabara, S.-A., J. Eyre, R. A. Anthes, and K. Holmlund, 2021: The Earth-observing satellite constellation: A review from a meteorological perspective of a complex, interconnected global system with extensive applications. *IEEE Geosci. Remote Sens. Mag.*, **9**, 26–42, https://doi.org/10.1109/MGRS.2021.3070248.

Calvo, N., R. R. Garcia, W. J. Randel, and D. R. Marsh, 2010: Dynamical mechanism for the increase in tropical upwelling in the lowermost tropical stratosphere during warm ENSO events. *J. Atmos. Sci.*, **67**, 2331–2340, https://doi.org/10.1175/2010JAS3433.1.

Calvo Fernández, N., R. R. García, R. García Herrera, D. Gallego Puyol, L. Gimeno Presa, E. Hernández Martín, and P. Ribera Rodríguez, 2004: Analysis of the ENSO signal in tropospheric and stratospheric temperatures observed by MSU, 1979–2000. *J. Climate*, **17**, 3934–3946, https://doi.org/10.1175/1520-0442(2004)017<3934:AOTESI>2.0.CO;2.

Capotondi, A., 2013: ENSO diversity in the NCAR CCSM4 climate model. *J. Geophys. Res. Oceans*, **118**, 4755–4770, https://doi.org/10.1002/jgrc.20335.

Chahine, M. T., and Coauthors, 2006: Improving weather forecasting and providing new data on greenhouse gases. *Bull. Amer. Meteor. Soc.*, **87**, 911–926, https://doi.org/10.1175/BAMS-87-7-911.

Chou, C., and M. H. Lo, 2007: Asymmetric responses of tropical precipitation during ENSO. *J. Climate*, **20**, 3411–3433, https://doi.org/10.1175/JCLI4197.1.

Compo, G. P., and P. D. Sardeshmukh, 2010: Removing ENSO-related variations from the climate record. *J. Climate*, **23**, 1957–1978, https://doi.org/10.1175/2009JCLI2735.1.

Feng, X., F. Xie, C. O. Ao, and R. A. Anthes, 2020: Ducting and biases of GPS radio occultation bending angle and refractivity in the moist lower troposphere. *J. Atmos. Oceanic Technol.*, **37**, 1013–1025, https://doi.org/10.1175/JTECH-D-19-0206.1.

Free, M., and D. J. Seidel, 2009: Observed El Niño–Southern Oscillation temperature signal in the stratosphere. *J. Geophys. Res.*, **114**, D23108, https://doi.org/10.1029/2009JD012420.

Gao, P., X. Xu, and X. Zhang, 2015: Characteristics of the trends in the global tropopause estimated from COSMIC radio occultation data. *IEEE Trans. Geosci. Remote Sens.*, **53**, 6813–6822, https://doi.org/10.1109/TGRS.2015.2449338.

Gettelman, A., and Coauthors, 2019: The Whole Atmosphere Community Climate Model version 6 (WACCM6). *J. Geophys. Res. Atmos.*, **124**, 12 380–12 403, https://doi.org/10.1029/2019JD030943.

Guan, B., and S. Nigam, 2008: Pacific sea surface temperatures in the twentieth century: An evolution-centric analysis of variability and trend. *J. Climate*, **21**, 2790–2809, https://doi.org/10.1175/2007JCLI2076.1.

Hersbach, H., and Coauthors, 2020: The ERA5 global reanalysis. *Quart. J. Roy. Meteor. Soc.*, **146**, 1999–2049, https://doi.org/10.1002/qj.3803.

Ho, S., and Coauthors, 2020: The COSMIC/FORMOSAT-3 radio occultation mission after 12 years: Accomplishments, remaining challenges, and potential impacts of COSMIC-2. *Bull.*

Amer. Meteor. Soc., **101**, E1107–E1136, https://doi.org/10.1175/BAMS-D-18-0290.1.

Johnston, B. R., F. Xie, and C. Liu, 2018: The effects of deep convection on regional temperature structure in the tropical upper troposphere and lower stratosphere. *J. Geophys. Res. Atmos.*, **123**, 1585–1603, https://doi.org/10.1002/2017JD027120.

——, W. J. Randel, and J. P. Sjoberg, 2021: Evaluation of tropospheric moisture characteristics among COSMIC-2, ERA5, and MERRA-2 in the tropics and subtropics. *Remote Sens.*, **13**, 880, https://doi.org/10.3390/rs13050880.

Kim, H. M., Y. Zhou, and M. A. Alexander, 2019: Changes in atmospheric rivers and moisture transport over the northeast Pacific and western North America in response to ENSO diversity. *Climate Dyn.*, **52**, 7375–7388, https://doi.org/10.1007/s00382-017-3598-9.

Kim, W., S. W. Yeh, J. H. Kim, J. S. Kug, and M. Kwon, 2011: The unique 2009–2010 El Niño event: A fast phase transition of warm pool El Niño to la Niña. *Geophys. Res. Lett.*, **38**, L15809, https://doi.org/10.1029/2011GL048521.

Kug, J.-S., F.-F. Jin, and S.-I. An, 2009: Two types of El Niño events: Cold tongue El Niño and warm pool El Niño. *J. Climate*, **22**, 1499–1515, https://doi.org/10.1175/2008JCLI2624.1.

L'Heureux, M. L., and Coauthors, 2017: Observing and predicting the 2015/16 El Niño. *Bull. Amer. Meteor. Soc.*, **98**, 1363–1382, https://doi.org/10.1175/BAMS-D-16-0009.1.

Liang, C. K., A. Eldering, A. Gettelman, B. Tian, S. Wong, E. J. Fetzer, and K. N. Liou, 2011: Record of tropical interannual variability of temperature and water vapor from a combined AIRS-MLS data set. *J. Geophys. Res.*, **116**, D06103, https://doi.org/10.1029/2010JD014841.

Liebmann, B., and C. A. Smith, 1996: Description of a complete (interpolated) outgoing longwave radiation dataset. *Bull. Amer. Meteor. Soc.*, **77**, 1275–1277, https://doi.org/10.1175/1520-0477-77.6.1274.

Liou, Y. A., and S. Ravindra Babu, 2020: ENSO signatures observed in tropical tropopause layer parameters using long-term COSMIC RO data. *GPS Solut.*, **24**, 98, https://doi.org/10.1007/s10291-020-01009-7.

Llamedo, P., R. Hierro, A. de la Torre, and P. Alexander, 2017: ENSO-related moisture and temperature anomalies over South America derived from GPS radio occultation profiles. *Int. J. Climatol.*, **37**, 268–275, https://doi.org/10.1002/joc.4702.

Luo, Z., D. Kley, R. H. Johnson, and H. Smit, 2008: Ten years of measurement of tropical upper-tropospheric water vapor by MOZAIC. Part II: Assessing the ECMWF humidity analysis. *J. Climate*, **21**, 1449–1466, https://doi.org/10.1175/2007JCLI1887.1.

Massie, S., A. Gettelman, W. Randel, and D. Baumgardner, 2002: Distribution of tropical cirrus in relation to convection. *J. Geophys. Res.*, **107**, 4591, https://doi.org/10.1029/2001JD001293.

McCarthy, M. P., P. W. Thorne, and H. A. Titchner, 2009: An analysis of tropospheric humidity trends from radiosondes. *J. Climate*, **22**, 5820–5838, https://doi.org/10.1175/2009JCLI2879.1.

NOAA Climate Prediction Center, 2021: Oceanic Niño Index. CPC, https://origin.cpc.ncep.noaa.gov/products/analysis_monitoring/ensostuff/ONI_v5.php.

Paek, H., J. Y. Yu, and C. Qian, 2017: Why were the 2015/2016 and 1997/1998 extreme El Niños different? *Geophys. Res. Lett.*, **44**, 1848–1856, https://doi.org/10.1002/2016GL071515.

Pan, L. L., S. B. Honomichl, T. Bui, T. Thornberry, A. Rollins, E. Hintsa, and E. J. Jensen, 2018: Lapse rate or cold point: The tropical tropopause identified by in situ trace gas measurements. *Geophys. Res. Lett.*, **45**, 10 756–10 763, https://doi.org/10.1029/2018GL079573.

Pearson, K. J., R. J. Hogan, R. P. Allan, G. M. S. Lister, and C. E. Holloway, 2010: Evaluation of the model representation of the evolution of convective systems using satellite observations of outgoing longwave radiation. *J. Geophys. Res.*, **115**, D20206, https://doi.org/10.1029/2010JD014265.

Pougatchev, N., and Coauthors, 2009: IASI temperature and water vapor retrievals—Error assessment and validation. *Atmos. Chem. Phys.*, **9**, 6453–6458, https://doi.org/10.5194/acp-9-6453-2009.

Randel, W. J., and M. Park, 2006: Deep convective influence on the Asian summer monsoon anticyclone and associated tracer variability observed with Atmospheric Infrared Sounder (AIRS). *J. Geophys. Res.*, **111**, D12314, https://doi.org/10.1029/2005JD006490.

——, and F. Wu, 2015: Variability of zonal mean tropical temperatures derived from a decade of GPS radio occultation data. *J. Atmos. Sci.*, **72**, 1261–1275, https://doi.org/10.1175/JAS-D-14-0216.1.

——, R. R. Garcia, N. Calvo, and D. Marsh, 2009: ENSO influence on zonal mean temperature and ozone in the tropical lower stratosphere. *Geophys. Res. Lett.*, **36**, L15822, https://doi.org/10.1029/2009GL039343.

Rieckh, T., R. Anthes, W. Randel, S. P. Ho, and U. Foelsche, 2018: Evaluating tropospheric humidity from GPS radio occultation, radiosonde, and AIRS from high-resolution time series. *Atmos. Meas. Tech.*, **11**, 3091–3109, https://doi.org/10.5194/amt-11-3091-2018.

Rocken, C., and Coauthors, 1997: Analysis and validation of GPS/MET data in the neutral atmosphere. *J. Geophys. Res.*, **102**, 29 849–29 866, https://doi.org/10.1029/97JD02400.

Ropelewski, C. F., and M. S. Halpert, 1987: Global and regional scale precipitation patterns associated with the El Niño/Southern Oscillation. *Mon. Wea. Rev.*, **115**, 1606–1626, https://doi.org/10.1175/1520-0493(1987)115<1606:GARSPP>2.0.CO;2.

Santer, B. D., and Coauthors, 2005: Amplification of surface temperature trends and variability in the tropical atmosphere. *Science*, **309**, 1551–1556, https://doi.org/10.1126/science.1114867.

Scherllin-Pirscher, B., C. Deser, S. P. Ho, C. Chou, W. Randel, and Y. H. Kuo, 2012: The vertical and spatial structure of ENSO in the upper troposphere and lower stratosphere from GPS radio occultation measurements. *Geophys. Res. Lett.*, **39**, 2–7, https://doi.org/10.1029/2012GL053071.

Seager, R., N. Harnik, Y. Kushnir, W. Robinson, and J. Miller, 2003: Mechanisms of hemispherically symmetric climate variability. *J. Climate*, **16**, 2960–2978, https://doi.org/10.1175/1520-0442(2003)016<2960:MOHSCV>2.0.CO;2.

——, ——, W. A. Robinson, Y. Kushnir, M. Ting, H. P. Huang, and J. Velez, 2005: Mechanisms of ENSO-forcing of hemispherically symmetric precipitation variability. *Quart. J. Roy. Meteor. Soc.*, **131**, 1501–1527, https://doi.org/10.1256/qj.04.96.

Semenov, E. K., V. S. Platonov, and E. Sokolikhina, 2012: Synoptic aspects of the catastrophic flood formation in the northeast of Australia during extreme La Niña 2010–2011. *Russ. Meteor. Hydrol.*, **37**, 90–97, https://doi.org/10.3103/S1068373912020033.

Smith, A. K., N. M. Pedatella, and Z. K. Mullen, 2020: Interhemispheric coupling mechanisms in the middle atmosphere of WACCM6. *J. Atmos. Sci.*, **77**, 1101–1118, https://doi.org/10.1175/JAS-D-19-0253.1.

Smith, E. K., and S. Weintraub, 1953: The constants in the equation for atmospheric refractive index at radio frequencies.

Proc. IRE, **41**, 1035–1037, https://doi.org/10.1109/JRPROC.1953.274297.

Sobel, A. H., I. M. Held, and C. S. Bretherton, 2002: The ENSO signal in tropical tropospheric temperature. *J. Climate*, **15**, 2702–2706, https://doi.org/10.1175/1520-0442(2002)015<2702:TESITT>2.0.CO;2.

Su, H., J. D. Neelin, and J. E. Meyerson, 2005: Mechanisms for lagged atmospheric response to ENSO SST forcing. *J. Climate*, **18**, 4195–4215, https://doi.org/10.1175/JCLI3514.1.

Takahashi, H., H. Su, and J. H. Jiang, 2016: Error analysis of upper tropospheric water vapor in CMIP5 models using "A-Train" satellite observations and reanalysis data. *Climate Dyn.*, **46**, 2787–2803, https://doi.org/10.1007/s00382-015-2732-9.

Teng, W. H., C. Y. Huang, S. P. Ho, Y. H. Kuo, and X. J. Zhou, 2013: Characteristics of global precipitable water in ENSO events revealed by COSMIC measurements. *J. Geophys. Res. Atmos.*, **118**, 8411–8425, https://doi.org/10.1002/jgrd.50371.

Tian, B., and T. Hearty, 2020: Estimating and removing the sampling biases of the AIRS Obs4MIPs V2 data. *Earth Space Sci.*, **7**, e2020EA001438, https://doi.org/10.1029/2020EA001438.

——, C. O. Ao, D. E. Waliser, E. J. Fetzer, A. J. Mannucci, and J. Teixeira, 2012: Intraseasonal temperature variability in the upper troposphere and lower stratosphere from the GPS radio occultation measurements. *J. Geophys. Res.*, **117**, D15110, https://doi.org/10.1029/2012JD017715.

——, E. J. Fetzer, B. H. Kahn, J. Teixeira, E. Manning, and T. Hearty, 2013: Evaluating CMIP5 models using AIRS tropospheric air temperature and specific humidity climatology. *J. Geophys. Res. Atmos.*, **118**, 114–134, https://doi.org/10.1029/2012JD018607.

Tian, E. W., H. Su, B. Tian, and J. H. Jiang, 2019: Interannual variations of water vapor in the tropical upper troposphere and the lower and middle stratosphere and their connections to ENSO and QBO. *Atmos. Chem. Phys.*, **19**, 9913–9926, https://doi.org/10.5194/acp-19-9913-2019.

Trenberth, K. E., J. M. Caron, D. P. Stepaniak, and S. Worley, 2002: Evolution of El Niño–Southern Oscillation and global atmospheric surface temperatures. *J. Geophys. Res.*, **107**, 4065, https://doi.org/10.1029/2000JD000298.

Wee, T. K., 2018: A variational regularization of Abel transform for GPS radio occultation. *Atmos. Meas. Tech.*, **11**, 1947–1969, https://doi.org/10.5194/amt-11-1947-2018.

Wyrtki, K., 1975: El Niño—The dynamic response of the equatorial Pacific Ocean to atmospheric forcing. *J. Phys. Oceanogr.*, **5**, 572–584, https://doi.org/10.1175/1520-0485(1975)005<0572:ENTDRO>2.0.CO;2.

Xie, F., D. L. Wu, C. O. Ao, and A. J. Mannucci, 2010: Atmospheric diurnal variations observed with GPS radio occultation soundings. *Atmos. Chem. Phys.*, **10**, 6889–6899, https://doi.org/10.5194/acp-10-6889-2010.

Xue, Y., J. Li, Z. Li, R. Lu, M. M. Gunshor, S. L. Moeller, D. Di, and T. J. Schmit, 2020: Assessment of upper tropospheric water vapor monthly variation in reanalyses with near-global homogenized 6.5-μm radiances from geostationary satellites. *J. Geophys. Res. Atmos.*, **125**, e2020JD032695, https://doi.org/10.1029/2020JD032695.

Yu, J. Y., and S. T. Kim, 2010: Identification of Central-Pacific and Eastern-Pacific types of ENSO in CMIP3 models. *Geophys. Res. Lett.*, **37**, L15705, https://doi.org/10.1029/2010GL044082.

Yu, X., F. Xie, and C. O. Ao, 2018: Evaluating the lower-tropospheric COSMIC GPS radio occultation sounding quality over the Arctic. *Atmos. Meas. Tech.*, **11**, 2051–2066, https://doi.org/10.5194/amt-11-2051-2018.

Yulaeva, E., and J. M. Wallace, 1994: The signature of ENSO in global temperature and precipitation fields derived from the Microwave Sounding Unit. *J. Climate*, **7**, 1719–1736, https://doi.org/10.1175/1520-0442(1994)007<1719:TSOEIG>2.0.CO;2.

Yun, K.-S., J.-Y. Lee, A. Timmermann, K. Stein, M. F. Stuecker, J. C. Fyfe, and E.-S. Chung, 2021: Increasing ENSO–rainfall variability due to changes in future tropical temperature–rainfall relationship. *Commun. Earth Environ.*, **2**, 4–11, https://doi.org/10.1038/s43247-021-00108-8.

Zeng, Z., S. Sokolovskiy, W. S. Schreiner, and D. Hunt, 2019: Representation of vertical atmospheric structures by radio occultation observations in the upper troposphere and lower stratosphere: Comparison to high-resolution radiosonde profiles. *J. Atmos. Oceanic Technol.*, **36**, 655–670, https://doi.org/10.1175/JTECH-D-18-0105.1.

Zhang, K., W. J. Randel, and R. Fu, 2017: Relationships between outgoing longwave radiation and diabatic heating in reanalyses. *Climate Dyn.*, **49**, 2911–2929, https://doi.org/10.1007/s00382-016-3501-0.

Zheng, F., L. Feng, and J. Zhu, 2015: An incursion of off-equatorial subsurface cold water and its role in triggering the "double dip" La Niña event of 2011. *Adv. Atmos. Sci.*, **32**, 731–742, https://doi.org/10.1007/s00376-014-4080-9.